Springer

Acta Mechanica Sinica

CrossMark click for updates

• RESEARCH PAPER •

Acta Mech. Sin., Vol. 38, 721489 (2022)
https://doi.org/10.1007/s10409-022-09032-x

Comparison between fully resolved and time-averaged simulations of particle cloud dispersion produced by a violent expiratory event

Akim Lavrinenko*, Alexandre Fabregat, and Jordi Pallares

Departament d'Enginyeria Mecánica, Universitat Rovira i Virgili, Spain, Av. Països Catalans, Tarragona 26, 43007, Spain

Received January 5, 2022; accepted January 30, 2022; published online April 25, 2022

In this work we compare the DNS results (Fabregat et al. 2021, Fabregat et al. 2021) for a mild cough already reported in the literarure with those obtained with a compressible URANS equations with a k-ϵ turbulence model. In both cases, the dispersed phase has been modelled as spherical Lagrangian particles using the one-way coupling assumption. Overall, the URANS model is capable of reproducing the observed tendency of light particles under 64 μm in diameter to rise due to the action of the drag exerted by the buoyant puff generated by the cough. Both DNS and URANS found that particles above 64 μm will tend to describe parabolic trajectories under the action of gravitational forces. Grid independence analysis allows to qualify the impact of increasing mesh resolution on the particle cloud statistics as flow evolves. Results suggest that the k-ϵ model overpredicts the horizontal displacement of the particles smaller than 64 μm while the opposite occurs for the particles larger than 64 μm.

CFD, Covid-19, DNS, URANS, Lagrangian particle tracking, Cough, Aerosol dispersion

Citation: A. Lavrinenko, A. Fabregat, and J. Pallares, Comparison between fully resolved and time-averaged simulations of particle cloud dispersion produced by a violent expiratory event, Acta Mech. Sin. **38**, 721489 (2022), https://doi.org/10.1007/s10409-022-09032-x

1. Introduction

Throughout history, mankind had to endure several pandemics that have cost many human lives and profoundly affected economic and social spheres on a global scale. In today's global world, the COVID-19 pandemic has had an enormous impact on our lives and has posed a major challenge to public health systems around the world. As of mid-2021 there have been approximately 200 million confirmed cases and just over 4 million deaths [1].

The flow physics plays a central role in the spreading of the infection that occurs when pathogen-laden droplets are spewed into the air when an infected person breathes, talks, coughs or sneezes [2]. Computational fluid dynamics (CFD) has been extensively used to shed some light on the factors that control the ability of these fluid particles to disperse in the environment after being released during respiratory events [3-11].

Mittal et al. [12] pointed out the existing scientific gaps in our understanding of the transmission pathways of respiratory diseases and the strategies for mitigating it. The airflow produced by violent respiratory events contains an average of approximately 25000 particles, as reported by Duguid [13]. Depending on their size and the underlying flow hydrodynamics, these pathogen-laden particles are capable of remaining afloat and disperse by the action of the background air motion enabling disease transmission. The World Health Organization (WHO) and the US Centers for Disease Control and Prevention (CDC) officially acknowledged inhalation of virus-laden aerosols as the main transmission route for SARS-CoV-2 [14, 15].

It is known that different factors such as ambient air humidity and velocity and temperature affect the dispersion and distance travelled by exhaled particles. Wells [16] was one of the first who studied how air humidity and droplet size influences droplet deposition time. Xie et al. [17] and

*Corresponding author. E-mail address: akim.lavrinenko@urv.cat (Akim Lavrinenko)
Executive Editor: Cristian Marchioli

later Chong et al. [18] continued Wells studies. Pendar and Páscoa [19] reported a detailed analysis of the transport characteristics and fluid dynamics for saliva droplets spewed during a sneeze in an indoor environment using a fully-coupled Eulerian-agrangian method. They concluded that the horizontal range of the particle cloud strongly depends on the ambient air conditions. Abkarian et al. [20] modeled a human cough using Large Eddy simulation (LES) with the Lagrangian particle approach in order to analyze flows during breathing and speaking considering the impact of phonetic features. They concluded that virus transmission is enhanced during rapid and excited speech, typical of social gatherings and singing events. The time spent in front of another person is a major factor, too: they recommend speakers to keep a distance of 2 m or more between them for conversations longer than 30 s. Bourouiba et al. [21] experimentally studied coughs and concluded that the turbulent hydrodynamics strongly affects the spatial range of the particle cloud. Dbouk and Drakakis et al. [22] reported that the region of influence of the particle cloud produced by a sneeze under windy conditions is 2-4 times larger than that in the absence of background flow. Their results suggest that, in open spaces, wind can enhance the transport of aerosols far beyond the 2-m separation, a distance considered as safe in many social distancing guidelines. In addition, human physiological factors may also affect the dispersion of the particle cloud. Fontes et al. [23] used Detached Eddy simulation (DES) to study a cough with different saliva properties and different geometries of the nasal and buccal passages. They suggested that differences in the anatomy of the nose and throat have a dramatic impact on the particle spray characteristics. More recently, and on the DNS front, Diwan [24] simulated the hydrodynamics evolution of the first 27.5 s of a dry cough with an in-house code using a mesh with 2.15 billion cells. The authors, however, provided limited results that could be readily used in a validation against URANS. Fabregat et al. [25, 26] also used DNS and Lagrangian particle tracking (LPT) to simulate the initial 1.67 s of a mild cough with evaporating and non-evaporating particles between 4 and 256 μm in diameter.

In this work, an unsteady compressible RANS simulation is used to repeat the exact same flow set-up used by Fabregat et al. [25, 26], who numerically investigate the idealized flow produced by mild cough, and compare the results with the DNS reported by these authors. In Ref. [26], it is shown that for for the selected initial conditions, flow setup and computational domain, the evaporation of the particles does not affect significantly particle cloud trajectory. Current study goal is to determine the deviations of the thermal puff and particle cloud trajectories introduced by modeling the turbulent transport using a k-ϵ model. Notably, the transient nature of the flow poses a challenge for URANS due to the transition from laminar to turbulent regimes as the air injection accelerates at the beginning of the cough event and also, later on, due to the turbulence intensity rapid decay once the exhalation has ceased.

All in all, COVID-19 has received a massive response from the research community in wide range of areas. On the CFD field, the need for reliable and computationally affordable methodologies to predict pathogen-laden particles dispersion is still an on-going challenge. This study should shed some light on the trade-off between CPU requirements and accuracy in predicting the dispersion of the aerosol cloud and results may be of interest for those who study numerically jet flows and particle dispersion and modelers who need benchmark results [27]. Also, results may be valuable, as initial conditions, for those interested in simulations of the long term dispersion of pathogen laden aerosols.

2. Physical and mathematical model

The numerical simulation of a violent expiatory event resembling a mild cough is carried out using OpenFoam with the reactingParcelFoam solver. This is a transient solver for compressible, turbulent flow equipped with a reacting multiphase particle module and surface film modelling [28]. This solver has been used to replicate the flow set-up used in Fabregat et al. [25, 26] who used DNS to investigate both the hydrodynamics and particle dispersion in idealized environments. Figure 1 shows a sketch of the computational domain with boundary conditions and coordinate system. The cough is modelled as a transient jet flow of air at constant temperature (34°C) with linearly increasing inlet velocity from 0 m s^{-1} up to 4.8 m s^{-1} at 0.15 s and then a linearly decreasing velocity to 0 m s^{-1} at 0.4 s. The air flow is ejected into a quiescent environment with a temperature of 15°C. Respiratory aerosols are modelled as solid spherical Lagrangian particles continuously ejected with the exhaled air over the duration of the exhalation. To facilitate the comparison of particle dispersion between the DNS in Fabregat et al. [26] and the URANS simulations, we considered here $n = 7$ different particle diameters in the range $2^{(j+1)}$ μm with $j = 1, 2, ..., n$. The exhaled air and the accompanying particles are injected through an inlet of circular section of 2 cm in diameter (see Fig. 1). The motion of the aerosol particles, assumed Lagrangian and spherical, is obtained by solving the set of ordinary differential equations governing their position and velocity. All particle sizes are ejected simultaneously during exhalation. Air is considered to be ideal gas with physical properties calculated using "Janaf polynomials" [29].

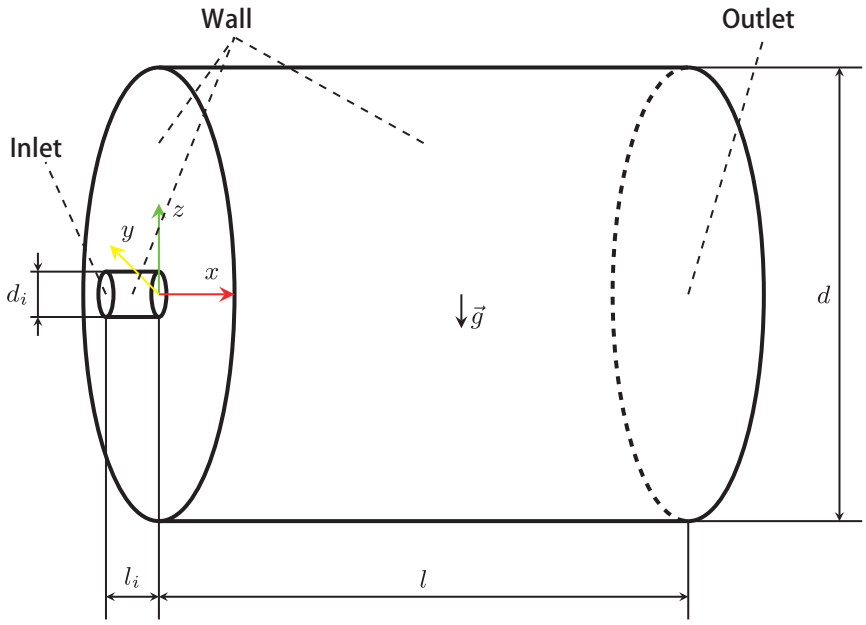

Figure 1 Sketch of the computational domain, l = 1.6 m, d = 1.0 m, l_i = 0.04 m, d_i = 0.02 m. The dimensions of the domain are the same as for the DNS of Fabregat et al. [26]

2.1 Carrier flow transport equations

ReactingParcelFoam solves numerically the system of density weighted time averaged Navier-Stokes equations [30]. The system including the continuity, the momentum and the energy equation [31], which can be written as

$$\frac{\partial \rho}{\partial t} + \frac{\partial}{\partial x_j}(\rho u_j) = 0, \tag{1}$$

$$\frac{\partial}{\partial t}(\rho u_i) + \frac{\partial}{\partial x_j}\left(\rho u_i u_j - \mu_{\text{eff}}\frac{\partial u_i}{\partial x_j}\right) = -\frac{\partial p}{\partial x_i} + \rho g \delta_{i3}, \tag{2}$$

$$\frac{\partial}{\partial t}(\rho h + \rho k) + \frac{\partial}{\partial x_j}\left(\rho u_j h + \rho u_j k - \alpha_{\text{eff}}\frac{\partial h}{\partial x_j}\right) = \frac{\partial p}{\partial x_j} + \rho u_j g \delta_{i3}. \tag{3}$$

In Eqs. (1)-(3), u_i is the i-th component of the density weighted time averaged velocity field in the x_i direction, p is pressure, t is time, u' is the fluctuating part of the velocity, δ_{i3} is the Kronecker delta, ρ is the air density, g is the gravitational acceleration, h is the density weighted time averaged enthalpy, k is kinetic energy, μ_{eff} is the effective viscosity (viscous + turbulent) α_{eff} is the effective thermal diffusivity (diffusive + turbulent).

2.2 Turbulence model

The standard k-ϵ turbulence model for compressible fluid in openFoam 8 has been used [32]. The turbulent kinetic energy dissipation rate and the turbulent kinetic energy are shown in Eqs. (4) and (5) respectively.

$$\begin{aligned}&\frac{\partial}{\partial t}(\rho\epsilon) + \frac{\partial}{\partial x_i}(\rho u\epsilon) - \frac{\partial^2}{\partial x_i^2}(\rho D_\epsilon \epsilon)\\ &= C_1 \rho G \frac{\epsilon}{k} - \left[\left(\frac{2}{3}C_1 - C_{3,RDT}\right)\rho\frac{\partial}{\partial x_i}u\epsilon\right] - \left(C_2\rho\frac{\epsilon}{k}\epsilon\right)\\ &\quad + S_\epsilon + S_{\text{fvOptions}},\end{aligned} \tag{4}$$

where G is turbulent kinetic energy production rate due to the anisotropic part of the Reynolds-stress tensor, D_ϵ is effective diffusivity for ϵ, C_1 and C_2 are model coefficients , $C_{3,RDT}$ is rapid-distortion theory compression term coefficient (Table 1), S_ϵ is internal source term for ϵ and $S_{\text{fvOptions}}$ is source terms introduced by fvOptions dictionary for ϵ.

$$\begin{aligned}&\frac{\partial}{\partial t}(\rho k) + \frac{\partial}{\partial x_i}(\rho u k) - \frac{\partial^2}{\partial x_i^2}(\rho D_\epsilon k)\\ &= \rho G - \left(\frac{2}{3}\rho\frac{\partial}{\partial x_i}uk\right) - \left(\rho\frac{\epsilon}{k}k\right) + S_k + S_{\text{fvOptions}},\end{aligned} \tag{5}$$

where S_k is internal source term for the k and $S_{\text{fvOptions}}$ is source terms introduced by fvOptions dictionary for k. Turbulence model coefficients are listed in Table 1.

Table 1 Default model coefficients

Coefficient	Value
C_μ	0.09
C_1	1.44
C_2	1.92
$C_{3,RDT}$	0.0
δ_k	1.0
δ_ϵ	1.3

2.3 Dispersed phase transport equations

A particle p is defined by the position of its center $\hat{x}$, its diameter $\hat{d}$, its velocity $\hat{u}_i$ and its density $\hat{\rho}$. For the dispersed phase, the particle motion is solved by integrating the force balance, which can be written in a Lagrangian frame [33]:

$$\frac{\partial \hat{x}_i}{\partial t} = \hat{u}_i, \tag{6}$$

$$\hat{m}\frac{\partial \hat{u}_i}{\partial t} = F_{d,i} + F_{g,i}\delta_{i3}, \tag{7}$$

where $\hat{m} = \frac{\hat{\rho}\hat{d}^3\pi}{6}$ is particle mass, $\hat{u}_i$ is particle velocity, $F_{d,i}$ is the particle drag force, $F_{g,i}$ is apparent weight.

Then spherical particle drag force is

$$F_{d,i} = \hat{m}_i\frac{u_i - \hat{u}_i}{\hat{\tau}}. \tag{8}$$

The relaxation time ($\hat{\tau}$) of the particles is the time it takes for a particle to respond to changes at the local flow velocity, and it is given by [33]

$$\hat{\tau} = \frac{4}{3}\frac{\hat{\rho}\hat{d}}{\rho C_d|u_i - \hat{u}_i|}. \tag{9}$$

The apparent weight is

$$F_{g,i} = (\hat{\rho} - \rho)g_i. \tag{10}$$

The drag coefficient C_d is a function of the particle Reynolds number ($\widehat{Re}$), which is defined as [33]

$$\widehat{Re} = \frac{\rho\hat{d}|u_i - \hat{u}_i|}{\mu}, \tag{11}$$

where μ is the dynamic viscosity of the fluid.

$$C_d = \begin{cases} \dfrac{24}{\widehat{Re}}, & \text{if } \widehat{Re} < 1, \\ \dfrac{24}{\widehat{Re}}(1 + \dfrac{3}{16}\widehat{Re}^{0.687}), & \text{if } 1 < \widehat{Re} < 5, \\ \dfrac{24}{\widehat{Re}}(1 + 0.15\widehat{Re}^{0.687}), & \text{if } 5 < \widehat{Re} < 1000, \\ 0.44, & \text{if } \widehat{Re} > 1000. \end{cases} \tag{12}$$

2.4 Computational grid

Seven different grid resolutions have been considered with the number of cells ranging between 1.8×10^5 and 1.7×10^7. Mesh is generated using the OpenFoam utility called blockMesh, which generates structured hexagonal meshes. The mesh resolution has been increased along the jet axis where larger gradients are expected. Mesh is also refined near the inlet and coarsened progressively along the x axis direction. As an example, Fig. 2 shows a mesh slice at $y = 0$ illustrating the grid cell distribution. Figure 2a shows the entire domain and Fig. 2b a detailed view near the inlet.

Table 2 lists the different cases, with the mesh details and computational cost. Meshes 1 and 2 simulations were carried out using on 8 core Intel(R) Core(TM) i7-6700 CPU @ 3.40GHz while mesh 3 to 7 used 24 core Intel Processor (Haswell, IBRS) 2.3 GHz.

3. Results

3.1 Grid-Independence test

The mesh resolution effect is illustrated in Fig. 3a-g that shows the instantaneous temperature field at $t = 1.5$ s sliced at $y = 0$ for each mesh listed in Table 2. Figure 3h shows, for comparison, the instantaneous temperature field from the DNS by Fabregat et al. [25] at the same time. The colorbar of the temperature field is shown at the bottom of Fig. 3. Results indicate that coarse meshes limit the dispersion of the puff resulting in higher values of temperature along the plume axis. As resolution increases, the temperature field becomes more complex exhibiting richer fine scale structures associated with enhanced mixing, shorter horizontal penetration and lower maximum temperatures.

Figure 4 shows the horizontal (a) and vertical (b) thermal field centroid coordinates (blue lines), the variance (red lines) and the size of the hot puff (black lines) for each mesh in Table 2 at $t = 1.5$ s. The thermal field centroid and variance have been computed as the first and second moment using Eqs. (13) and (14) respectively. The horizontal puff size is determined as the maximum value of the x-coordinate where temperature is above the background unperturbed value. Analogously, the vertical puff size is computed as the difference between the maximum and minimum values of the y-coordinate above which temperature is larger than that corresponding to the unperturbed environment. For comparison purposes, dashed lines indicate the DNS predictions of the thermal puff size, centroid location and variance using the corresponding colors.

$$\tilde{x}_i = \frac{\int_V x_i T \mathrm{d}V}{\int_V T \mathrm{d}V}, \tag{13}$$

$$\tilde{\sigma}_i = \frac{\int_V (x_i - \tilde{x}_i)^2 T \mathrm{d}V}{\int_V T \mathrm{d}V}. \tag{14}$$

In Eqs. (13) and (14), $\tilde{x}_i$ and σ_i are first and second moments (centroid and variance) in each direction i, V is the volume of the computational domain, T is temperature field and x_i is the horizontal or vertical coordinate.

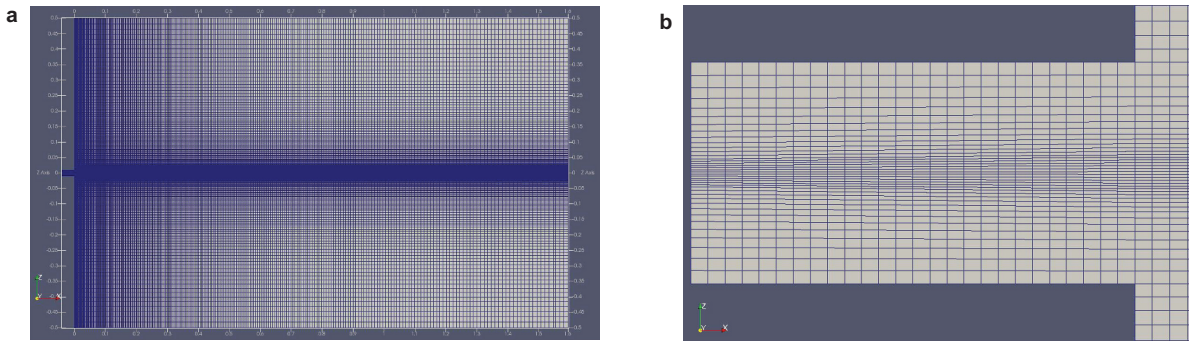

Figure 2 Computational domain slice at $Y = 0$, Mesh 3 (see Table 2). **a** Whole domain; **b** inlet pipe.

Table 2 Mesh details and simulation time for the mesh independence study. CPU hours are calculated for simulation time equal to t=1.5 s. In parenthesis, the used CPU configuration is specified where 1 stands for Intel(R) Core(TM) i7-6700 CPU@3.40GHz and 2 for 24 core Intel Processor (Haswell, IBRS) 2.3 GHz. Min cell is the cube root of minimal cell volume and max cell is the cube root of maximal cell volume, Avg non-ortho is average mesh non-orthogonality.

Mesh ID	Cell count ($\times 10^6$)	CPU-hours	Min cell (m $\times 10^{-4}$)	Max cell (m $\times 10^{-2}$)	Max skewness	avg non-ortho
Mesh 1	0.18	3.49×10^2(1)	6.61	5.12	0.65	2.99
Mesh 2	0.51	4.41×10^3(1)	4.40	3.61	0.69	3.20
Mesh 3	1.0	3.22×10^3(2)	3.27	2.79	0.72	3.31
Mesh 4	3.0	2.92×10^4(2)	2.32	1.96	0.75	3.2
Mesh 5	6.0	2.19×10^4(2)	1.87	1.60	0.76	3.21
Mesh 6	10.0	9.29×10^4(2)	1.56	1.34	0.77	3.22
Mesh 7	17.0	2.66×10^5(2)	1.28	1.12	0.77	3.24

Results in Fig. 4 show that the values of puff size (black lines) only settle when the mesh resolution is above that used in Mesh 5, namely, 6 million cells. In contrast to the thermal puff sizes, horizontal and vertical centroid coordinates (in blue) exhibit a slight tendency to keep decreasing as the resolution increases. The variance of the thermal field, used as a proxy for the thermal puff horizontal and vertical widths, are found to reach a plateau when resolution 1 million cells.

In comparison to the DNS values in Ref. [25], URANS results for both metrics intended to measure the horizontal range attained by the penetrating plume, namely the thermal puff size and the variance, seems to slightly overpredict the DNS results. The larger horizontal centroid coordinate obtained with URANS indicates that this approach tends also to predict a further penetration of the thermal field. All in all, these results suggest that the URANS simulation underpredicts the horizontal turbulent mixing for this flow configuration. Notably, results in Fig. 4b show that URANS underpredicts the vertical thermal puff extent while both the centroid and variance predictions are relatively close to those obtained in the DNS.

3.2 Main results

A snapshot of the particle cloud at the end of the URANS simulation (t = 1.7 s) is shown in Fig. 5 for Mesh 3 (a), Mesh 6 (b) and Mesh 7 (c). Each color represents a particle size ranging from red (4 μm) to magenta (256 μm). At t = 1.7 s almost all the large particles with the diameters of 256 and 128 μm have reached the bottom boundary of the computational domain. On the other hand, particles with diameters of 4 and 16 μm show ascending trajectories due to the updrafting buoyant puff while intermediate sizes of 32 and 64 μm remain afloat while describing slightly descending trajectories. Increasing mesh resolutions from Meshes 3, 6 and 7 leads to a richer particle cloud topology as a results of the finer scales that emerge when the flow hydrodynamics is better resolved. Notably though, the general features and relative positions of every particle size cloud remain pretty similar despite the one order of magnitude difference in the number of cells.

The mesh resolution effect on the particle cloud dispersion is better observed in the temporal evolution of the particle positions projected along the y axis shown in Fig. 6. Each snapshot shows the particle positions (for all sizes) at times t = 0.2 s (a), t = 0.4 s (b), t = 1.0 s (c) and t = 1.7 s (d). Blue, red and green colors correspond to three different selected grid resolutions, namely Meshes 3, 6 and 7, respectively (see Table 2).

Results suggest that as the mesh resolution and time increase, the particle cloud dispersion is enhanced and axial cloud penetration along the axial direction decrease. The signature of the finer flow features that emerge as resolution increases is clearly observed in the green cloud that exhibits

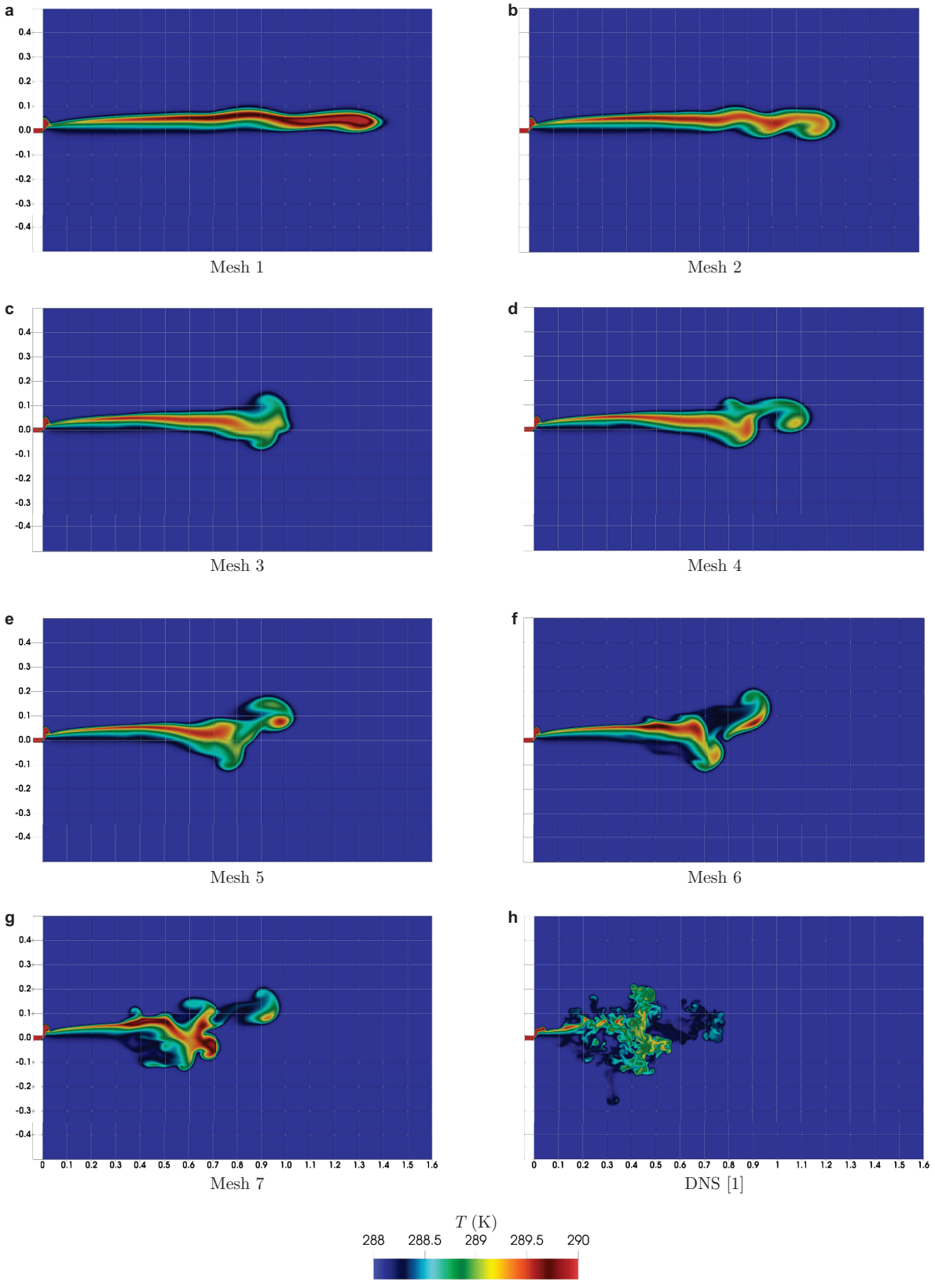

Figure 3 Instantaneous contours of temperature at $Y = 0$ and at $t = 1.5$ s (for mesh resolution details see Table 2)

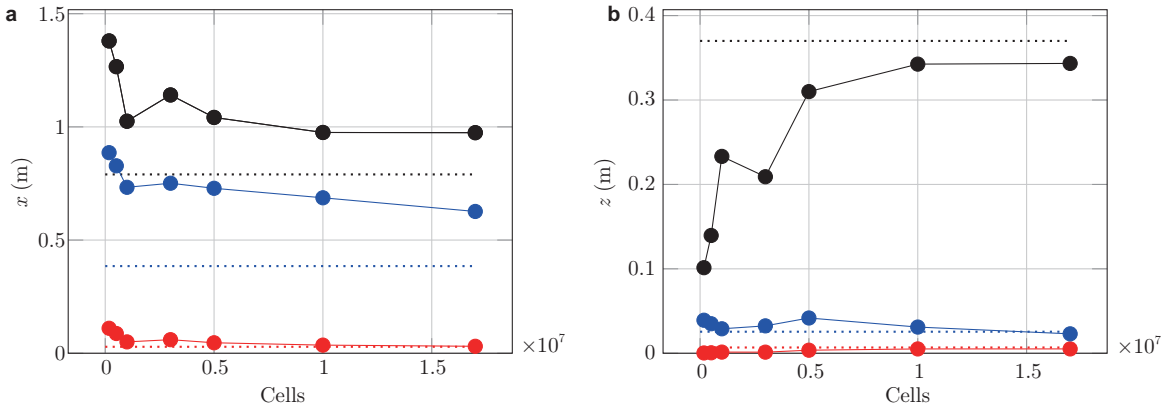

Figure 4 Horizontal **a** and vertical **b** puff size (black), centroid position (blue) and variance (red) at t = 1.5 s as a function of the mesh resolution. Dashed line indicate DNS results from Fabregat et al. [25].

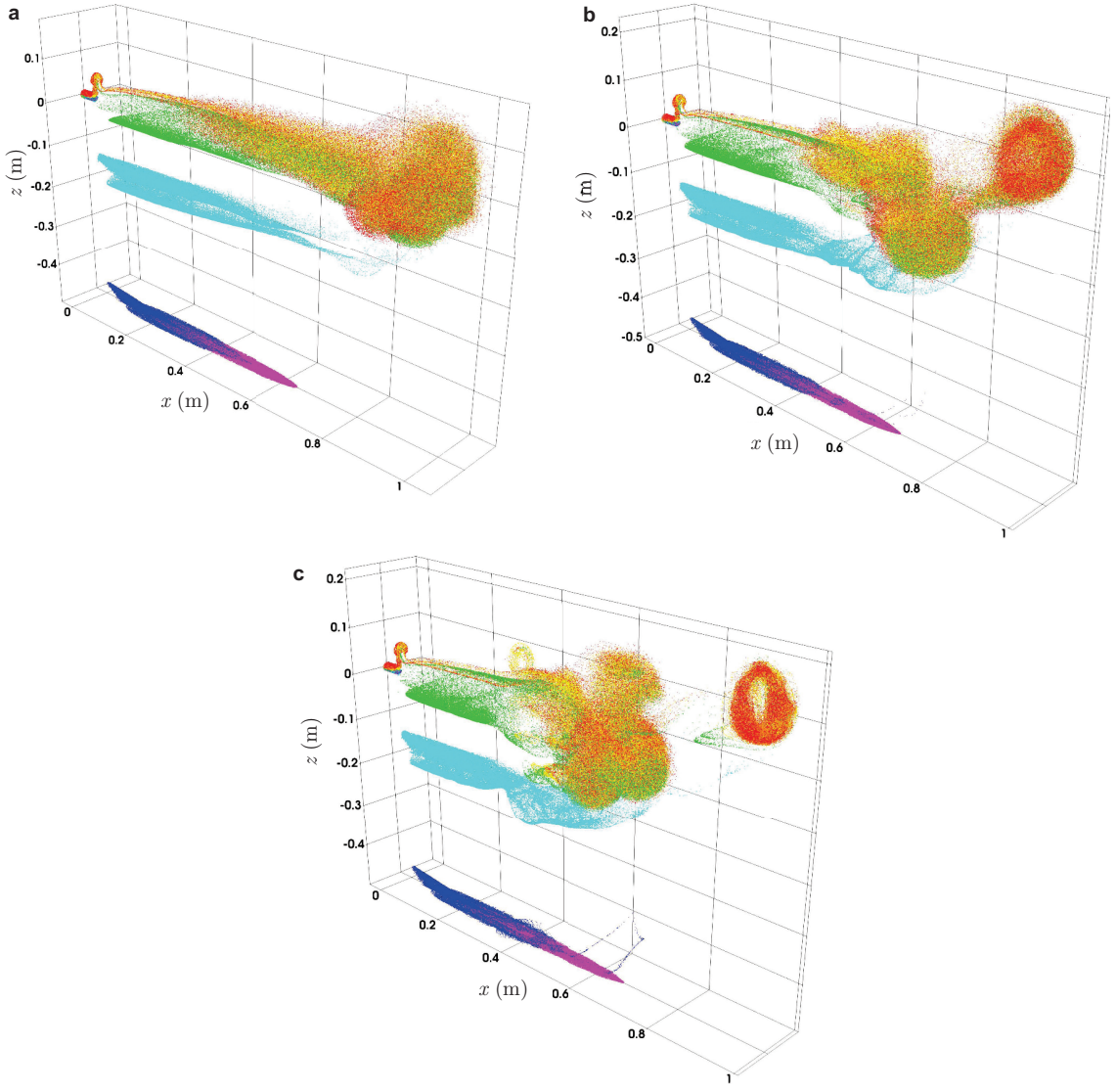

Figure 5 Snapshot of the particle cloud at t = 1.7 s, for Mesh 3 **a**, Mesh 6 **b** and Mesh 7 **c**. Colors indicate particle diameter: red 4 μm, orange 8 μm, yellow 16 μm, green 32 μm, cyan 64 μm, blue 128 μm, magenta 256 μm.

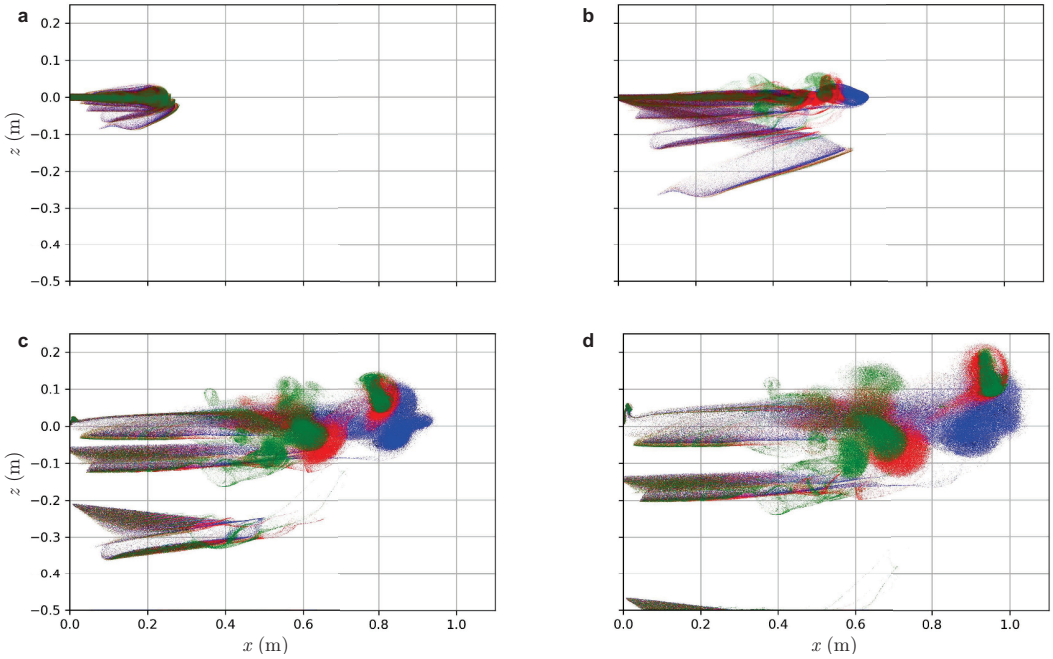

Figure 6 Snapshots of particle clouds at $t = 0.2$ s **a**, $t = 0.4$ s **b**, $t = 1.0$ s **c** and $t = 1.7$ s **d** produced by simulations with different mesh resolution. Blue, red and green colors represent Meshes 3, 6 and 7, respectively (for mesh details see Table 2).

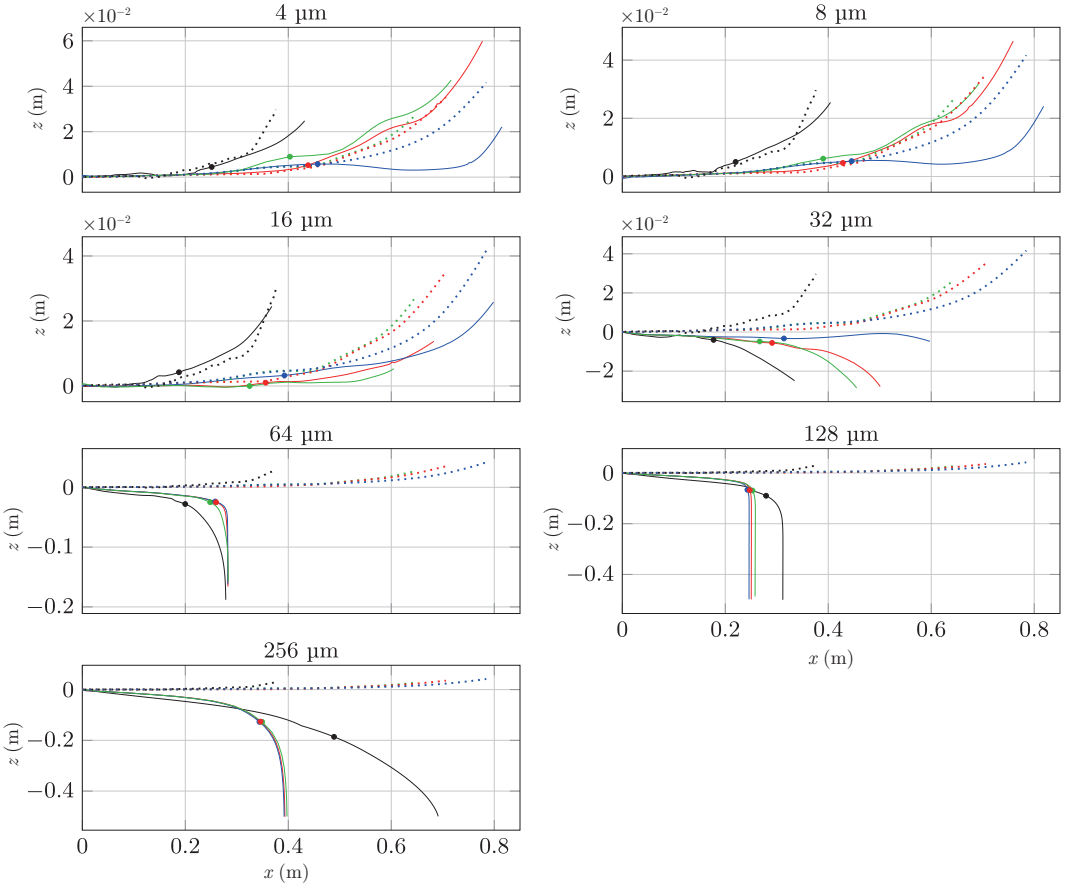

Figure 7 Trajectories of the particle cloud and puff centroids. Lines represents particle cloud trajectory and dashed lines thermal puff trajectory. DNS results are plotted in black. Blue, red and green denotes URANS with Meshes 3, 6 and 7, respectively. The markers in the trajectories of the particle cloud indicate the particle cloud centroid position at the end of the injection ($t = 0.4$ s).

more convoluted and complex distribution of particle positions in comparison to smaller cell count meshes.

The trajectories of the centroid of the thermal field (dashed line) and the particle cloud (solid line) are shown in Fig. 7. DNS predictions by Fabregat et al. [25, 26] are plotted in black and the present URANS simulations are plotted in blue, red and green for Meshes 3, 6 and 7 respectively. Dot markers indicate the end time of the air injection (t = 0.4 s). The centroid trajectory of the particle cloud is determined as the average coordinates of all airborne particles after discarding those that deposited on the inlet pipe walls. Thermal puff trajectory is calculated using Eq. (13) at each time step.

The transport of the particles between 4 and 16 μm in diameter is dominated by hydrodynamic drag. As a result, the trajectory of the centroid exhibits a vertical deflection imposed by the vertical rising motion of the buoyant puff engulfing them. On the other hand, the particles larger than 64 μm in diameter are dominated by gravitational effects and exhibit a quasi-ballistic trajectories. For lighter particles with diameters from 4 μm to 16 μm URANS overpredicts the travel distance almost by factor of two. The travel distance of the particles with diameter 32 and 64 μm is close to that predicted by DNS. Particles with diameter 64 μm have closest trajectory to the DNS result. URANS underpredicts the travel distance compared to the DNS for particles with diameters 128 and 256 μm. For the latter, the average distance traveled by particles is almost twice smaller.

Figures 8 and 9 show the time evolution of the horizontal and vertical mean velocity of particle cloud over time for each particle size. DNS results are shown in black while

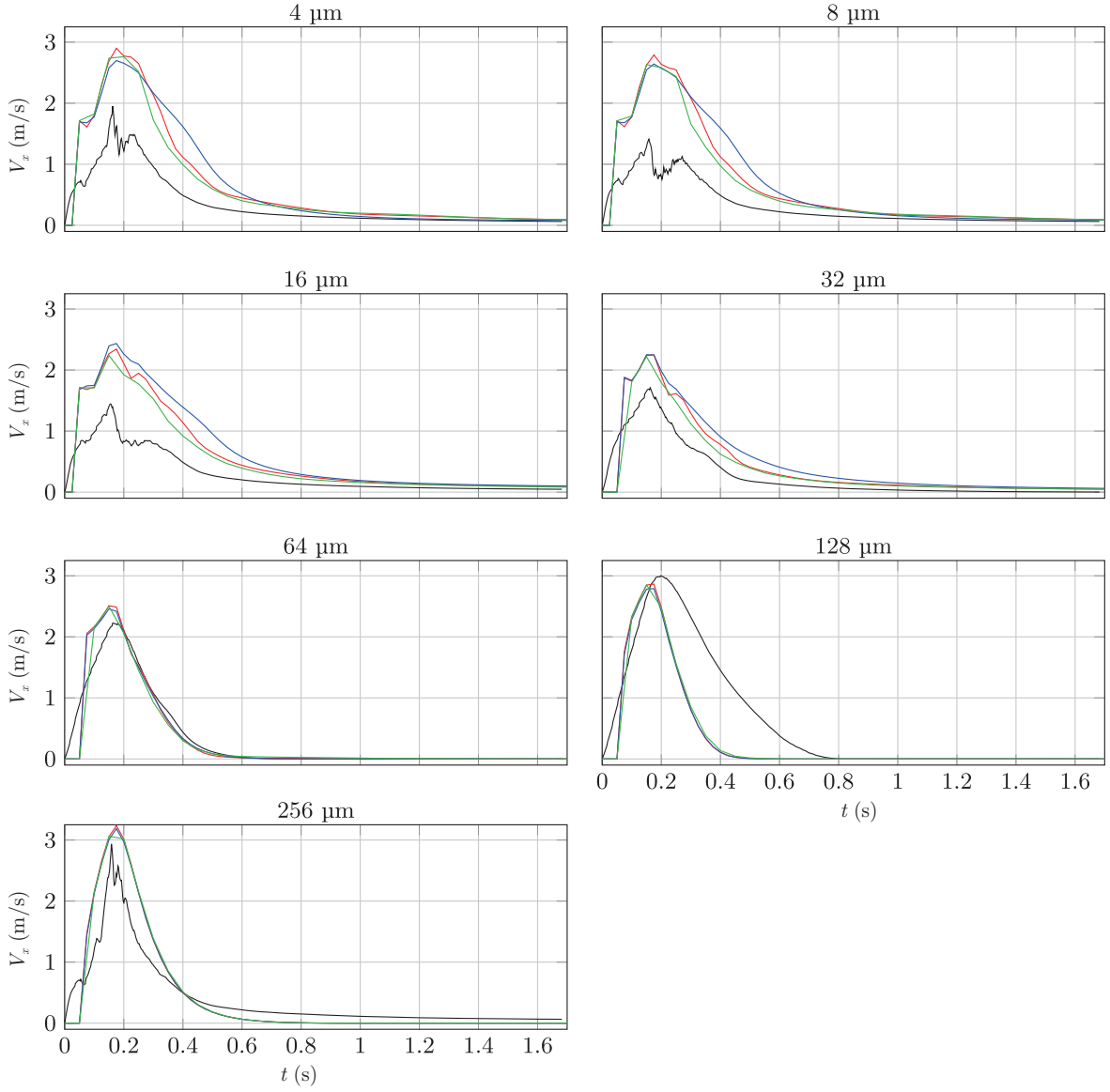

Figure 8 Horizontal velocity of particle cloud over time. Black, blue, red and green line indicates DNS, Meshes 3, 6 and 7, respectively.

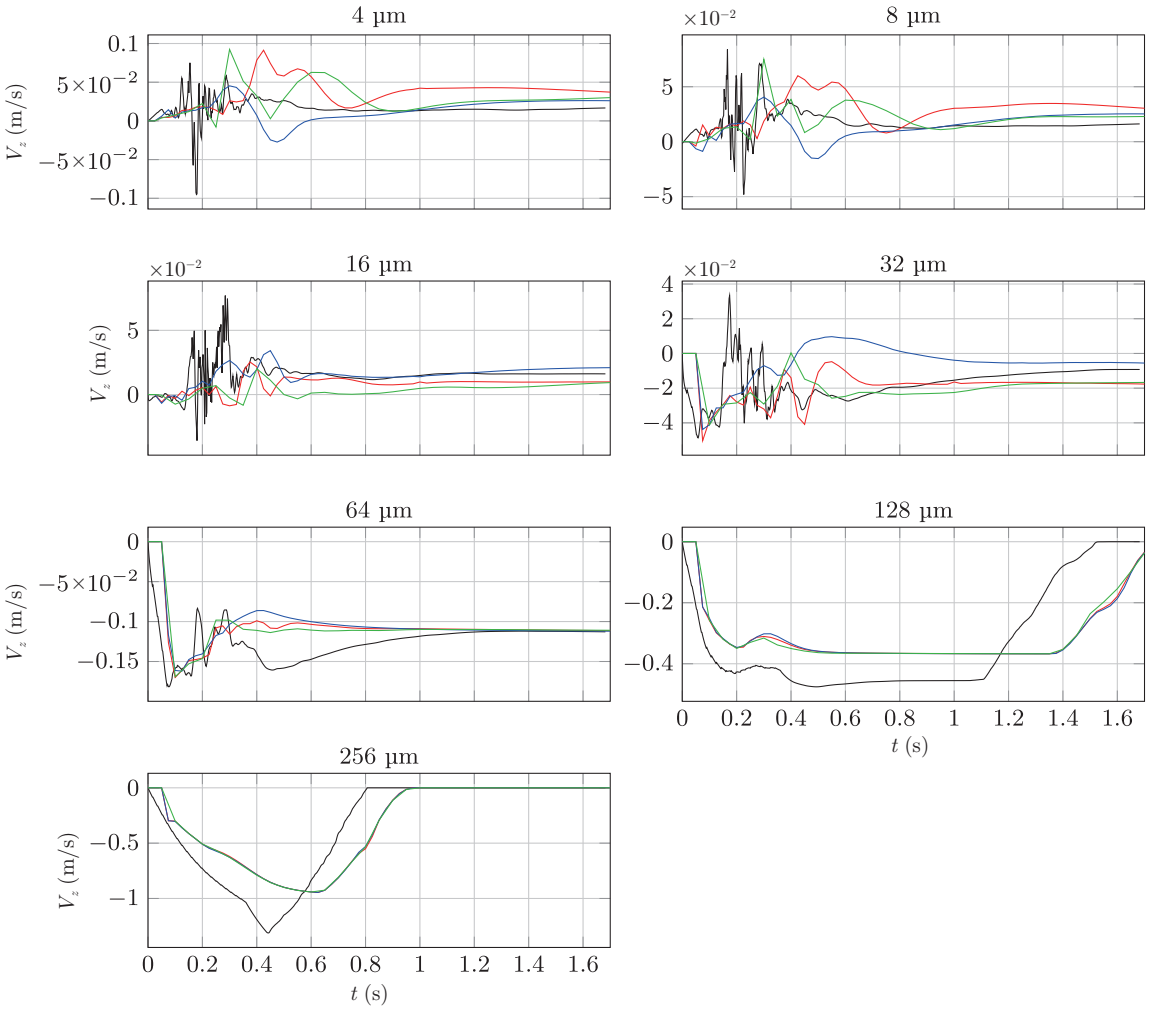

Figure 9 Vertical velocity of particle cloud over time. Black, blue, red and green line indicates DNS, Meshes 3, 6 and 7, respectively.

blue, red and green colors correspond URANS results with Meshes 3, 6 and 7 respectively. In URANS simulations particles leave inlet pipe after t=0.05 s therefore velocity increases not from the beginning of the injection because particles in the inlet pipe are not taken into consideration. In the DNS particles are released at X = 0.0 m [26]. In Fig. 9, when the mean particle cloud velocity is 0 m s^{-1} indicates that all particles has fallen to the bottom boundary of the computational domain. Figure 8 shows that, in comparison to DNS, URANS tends to overpredict the horizontal particle velocity for diameters under 64 µm resulting in larger horizontal ranges as shown in Fig. 7. Regarding particles of 64 µm, URANS and the DNS predictions of horizontal velocity and range are very similar. In contrast, URANS is found to underpredict the horizontal spread of particles with diameter of 128 µm regardless of the mesh resolution. URANS horizontal velocity predictions for the largest particles of 256 µm are in agreement to the DNS results. However, the URANS cloud centroid trajectory departs significantly from the DNS result.

Particles with diameters from 4 µm to 32 µm in Fig. 9 have higher vertical velocities in case of URANS. Vertical velocity of particles with diameter 64 µm converge with the DNS at t = 1.2 s. Both 128 and 256 µm particles vertical mean velocities are slightly lower in case of URANS and as a result particles reach the bottom boundary later as shown in Fig. 7.

4. Conclusion

In this study we used unsteady Reynolds-Averaged Navier-Stokes (URANS) equations to numerically simulate an idealized mild cough modelled as a transient injection of warm air into an initially quiescent colder environment. The rapid air exhalation is accompanied by the injection of spherical particles intended to represent the aerosols spewed into the air when a person coughs. By comparison to existing DNS databases [25] for the exact same flow set-up, we concluded

that URANS is fairly capable of reproducing the general features of the flow hydrodynamics and provide moderately good estimates of the aerosol cloud dispersion. This is relevant given the complex and transient nature of the flow characterized by (i) a laminar to turbulent regime transition during the accelerated air injection and (ii) the rapid turbulence intensity decay once the exhalation has ceased.

Mesh independence analysis allowed to quantify the effect of the cell count on the flow hydrodynamics which, in turn, dominates the particle cloud dispersion specially when the particles are small enough and drag dominates their transport. The impact of the emergence of finer flow features as the mesh resolution increases affecting the hydrodynamics and the turbulent mixing intensity has been quantitatively investigated using several metrics including the thermal field and particle cloud centroid position and variance. Specifically, we found that, as hydrodynamics are better resolved, the trajectory of the particle cloud centroid for diameters in the 4 μm to 32 μm range are closer to those reported in the DNS database [26]. Due to its ability to leave the thermal puff due to gravitational effects, particles above 32 μm in diameter are found to be insensitive to mesh resolution. However, for the meshes considered, the relative positions of every particle size cloud remain pretty similar despite the one order of magnitude difference between the coarsest and finest grids. URANS is found to overpredict the travelled distance of the particles with diameters from 4 μm to 32 μm and otherwise for particle diameters above 64 μm.

This work was supported by Spanish Ministerio de Ciencia, Innovación y Universidades (Grants Nos. RTI2018-100907-A-I00 and PID2020-113303GB-C21), and the Generalitat de Catalunya (Grant No. 2017-SGR-1234).

1 Coronavirus cases, https://www.worldometers.info/coronavirus/coronavirus-cases/.
2 V. Stadnytskyi, C. E. Bax, A. Bax, and P. Anfinrud, The airborne lifetime of small speech droplets and their potential importance in SARS-CoV-2 transmission, Proc. Natl. Acad. Sci. USA **117**, 11875 (2020).
3 A. A. Aliabadi, S. Rogak, S. Green, and K. Bartlett, in Cfd simulation of human coughs and sneezes: A study in droplet dispersion, heat, and mass transfer: Proceedings of the ASME International Mechanical Engineering Congress and Exposition (IMECE), Vancouver, 2010.
4 C. Chen, and B. Zhao, Some questions on dispersion of human exhaled droplets in ventilation room: answers from numerical investigation, Indoor Air **20**, 95 (2010).
5 J. Redrow, S. Mao, I. Celik, J. A. Posada, and Z. Feng, Modeling the evaporation and dispersion of airborne sputum droplets expelled from a human cough, Building Environ. **46**, 2042 (2011).
6 C. Paz, E. Suárez, and J. Vence, CFD transient simulation of the cough clearance process using an Eulerian wall film model, Comput. Methods BioMech. BioMed. Eng. **20**, 142 (2017).
7 G. Kou, X. Li, Y. Wang, M. Lin, Y. Zeng, X. Yang, Y. Yang, Z. Gan, Cfd simulation of airflow dynamics during cough based on ct-scanned respiratory airway geometries, Symmetry **10**, 595 (2018).
8 Z. Li, H. Wang, X. Zhang, T. Wu, and X. Yang, Effects of space sizes on the dispersion of cough-generated droplets from a walking person, Phys. Fluids **32**, 121705 (2020), arXiv: 2010.13348.
9 B. Zhang, G. Guo, C. Zhu, Z. Ji, and C. H. Lin, Transport and trajectory of cough-induced bimodal aerosol in an air-conditioned space, Indoor Built Environ. **30**, 1546 (2021).
10 H. Ge, L. Chen, C. Xu, and X. Cui, Large-eddy simulation of droplet-laden cough jets with a realistic manikin model, Indoor Built Environ. 1420326X2110322 (2021).
11 J. Wang, M. Alipour, G. Soligo, A. Roccon, M. De Paoli, F. Picano, and A. Soldati, Short-range exposure to airborne virus transmission and current guidelines, Proc. Natl. Acad. Sci. USA **118**, 2105279118 (2021).
12 R. Mittal, R. Ni, and J. H. Seo, The flow physics of COVID-19, J. Fluid Mech. **894**, F2 (2020), arXiv: 2004.09354.
13 J. Duguid, The numbers and the sites of origin of the droplets expelled during expiratory activities, Edinburgh Med. J. **52**, 385 (1945).
14 Coronavirus disease (covid-19): How is it transmitted? https://www.who.int/news-room/q-a-detail/coronavirus-disease-covid-19-how-is-it-transmitted.
15 Scientific brief: Sars-cov-2 transmission, https://www.cdc.gov/coronavirus/2019-ncov/science/science-briefs/sars-cov-2-transmission.html.
16 W. F. Wells, On air-borne infection, Am. J. Epidemiol. **20**, 611 (1934).
17 X. Xie, Y. Li, A. T. Y. Chwang, P. L. Ho, and W. H. Seto, How far droplets can move in indoor environments—revisiting the Wells evaporation—falling curve, Indoor Air **17**, 211 (2007).
18 K. L. Chong, C. S. Ng, N. Hori, R. Yang, R. Verzicco, and D. Lohse, Extended lifetime of respiratory droplets in a turbulent vapor puff and its implications on airborne disease transmission, Phys. Rev. Lett. **126**, 034502 (2021), arXiv: 2008.01841.
19 M. R. Pendar, and J. C. Páscoa, Numerical modeling of the distribution of virus carrying saliva droplets during sneeze and cough, Phys. Fluids **32**, 083305 (2020).
20 M. Abkarian, S. Mendez, N. Xue, F. Yang, and H. A. Stone, Speech can produce jet-like transport relevant to asymptomatic spreading of virus, Proc. Natl. Acad. Sci. USA **117**, 25237 (2020), arXiv: 2006.10671.
21 L. Bourouiba, E. Dehandschoewercker, and J. W. M. Bush, Violent expiratory events: On coughing and sneezing, J. Fluid Mech. **745**, 537 (2014).
22 T. Dbouk, and D. Drikakis, On coughing and airborne droplet transmission to humans, Phys. Fluids **32**, 053310 (2020).
23 D. Fontes, J. Reyes, K. Ahmed, and M. Kinzel, A study of fluid dynamics and human physiology factors driving droplet dispersion from a human sneeze, Phys. Fluids **32**, 111904 (2020).
24 S. S. Diwan, S. Ravichandran, R. Govindarajan, and R. Narasimha, Understanding transmission dynamics of COVID-19-type infections by direct numerical simulations of cough/sneeze flows, Trans Ind. Natl. Acad. Eng. **5**, 255 (2020).
25 A. Fabregat, F. Gisbert, A. Vernet, S. Dutta, K. Mittal, and J. Pallarès, Direct numerical simulation of the turbulent flow generated during a violent expiratory event, Phys. Fluids **33**, 035122 (2021).
26 A. Fabregat, F. Gisbert, A. Vernet, J. A. Ferré, K. Mittal, S. Dutta, and J. Pallarès, Direct numerical simulation of turbulent dispersion of evaporative aerosol clouds produced by an intense expiratory event, Phys. Fluids **33**, 033329 (2021).
27 J. Pallares, and A. Fabregat, A model to predict the short-term turbulent indoor dispersion of small droplets and droplet nuclei released from coughs and sneezes, Indoor Built Environ. 1420326X2110600 (2022).
28 Openfoam api guide reactingparcelfoam solver, https://www.openfoam.com/documentation/guides/latest/doc/guide-applications-solvers-lagrangian-reactingParcelFoam.html.
29 J. N. e. a. Bahram Haddadi, Christian Jordan. Openfoam basic training: Tutorial eleven, reactingfoam, 2015, https://www.cfd.at/sites/default/files/tutorials/2014_OFoam_Tut_Example.
30 Favre averaged navier-stokes equations, https://www.cfd-online.com/

Wiki/Favre_averaged_Navier-Stokes_equations.
31 J. Zhang, Modifying coalChemistryFoam for dense gas-solid simulation: Proceedings of CFD with OpenSource Software, 2018, edited by H. Nilsson, http://dx.doi.org/10.17196/OS_CFD#YEAR_2018.
32 k-epsilon turbulence model, https://www.openfoam.com/documentation/guides/latest/doc/guide-turbulence-ras-k-epsilon.html.
33 J. Xu, Modification of stochastic model in Lagrangian tracking method: Proceedings of CFD with OpenSource Software, 2016, edited by H. Nilsson, http://www.tfd.chalmers.se/~hani/kurser/OS_CFD_2016.

粒子云扩散完全解析和时间平均模拟的比较

Akim Lavrinenko, Alexandre Fabregat, Jordi Pallares

摘要 本文将现有文献中轻度咳嗽的直接数值模拟(DNS)结果与k-ϵ模型的可压缩非定常雷诺平均N-S (URANS)方程得到的结果进行了比较. 两种情况均采用单向耦合假设, 将分散相模拟为球形拉格朗日粒子. URANS模型能够再现轻粒子(粒径小于64 μm)的上升趋势, 这归因于咳嗽所产生浮力的阻力作用. 通过分析DNS和URANS的模拟结果发现, 在重力作用下, 大于64 μm的粒子倾向于描述抛物线轨迹. 网格独立性分析允许随着流动的发展, 确定网格分辨率的增加对粒子云统计数据的影响. 结果表明, k-ϵ模型过度预测了直径小于64 μm颗粒的水平位移而对于大于64 μm颗粒的预测则相反.